nature portfolio

https://doi.org/10.1038/s41586-024-07553-3

Supplementary information

Superconductivity in pressurized trilayer $La_4Ni_3O_{10-\delta}$ single crystals

In the format provided by the authors and unedited

Supplementary Information for

Superconductivity in pressurized trilayer $La_4Ni_3O_{10-\delta}$ single crystals

Contents

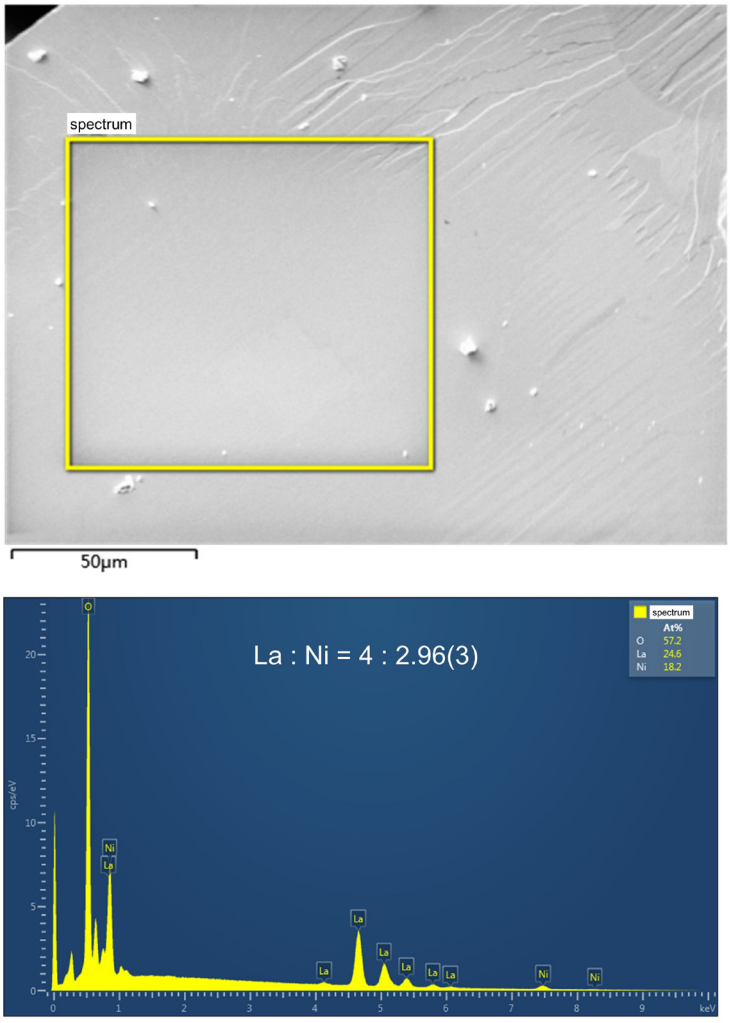

Supplementary Fig. 1 | Chemical composition analysis using a scanning electron microscope (SEM) equipped with energy-dispersive X-ray (EDX) spectroscopy on a selected area of a $La_4Ni_3O_{10-\delta}$ single crystal. The analysis reveals a La to Ni atomic ratio of approximately 4 : 2.96(3), aligning with findings from neutron diffraction, X-ray diffraction refinements, and scanning transmission electron microscopy (STEM) investigations. This consistency underscores the accuracy of the material's stoichiometry as determined by multiple advanced imaging and analysis techniques.

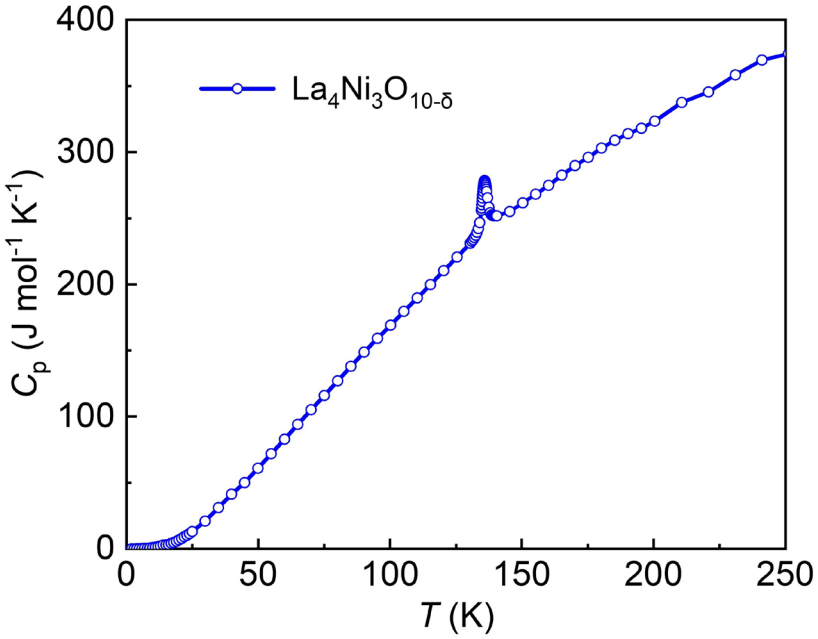

Supplementary Fig. 2| Temperature dependence of specific heat of a $La_4Ni_3O_{10-\delta}$ single crystal. A distinct feature corresponding to the spin density wave and charge density wave phase transition is clearly observable.

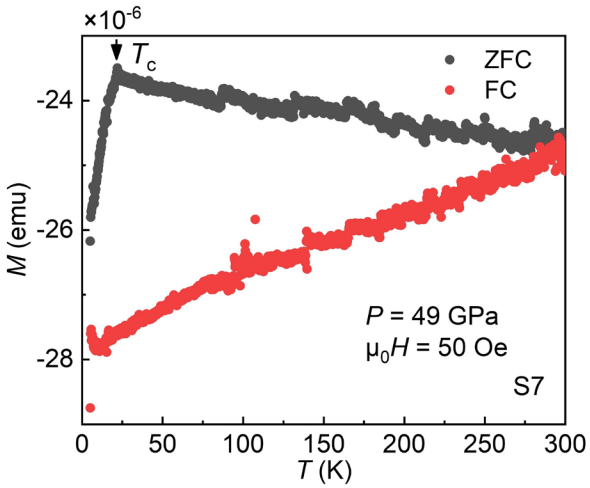

Supplementary Fig. 3 | Temperature dependent magnetization curves of $La_4Ni_3O_{10-\delta}$ under a magnetic field of 20 Oe applied perpendicular to the *ab* plane using the zero-field-cooled (ZFC) and field-cooled (FC) modes at 49.0 GPa for sample 7 (S7). A distinct superconducting diamagnetic response at T_c is clearly observed in the ZFC curve. The normal state signals are predominantly influenced by the contribution from the pressure cell. The splitting of ZFC and FC curve in the normal state at the terminated temperature of 300 K is due to the presence of magnetic impurities from the pressure cell, which can be seen clearly in the empty cell runs at different temperatures (Supplementary Figure 5, ref. 49).

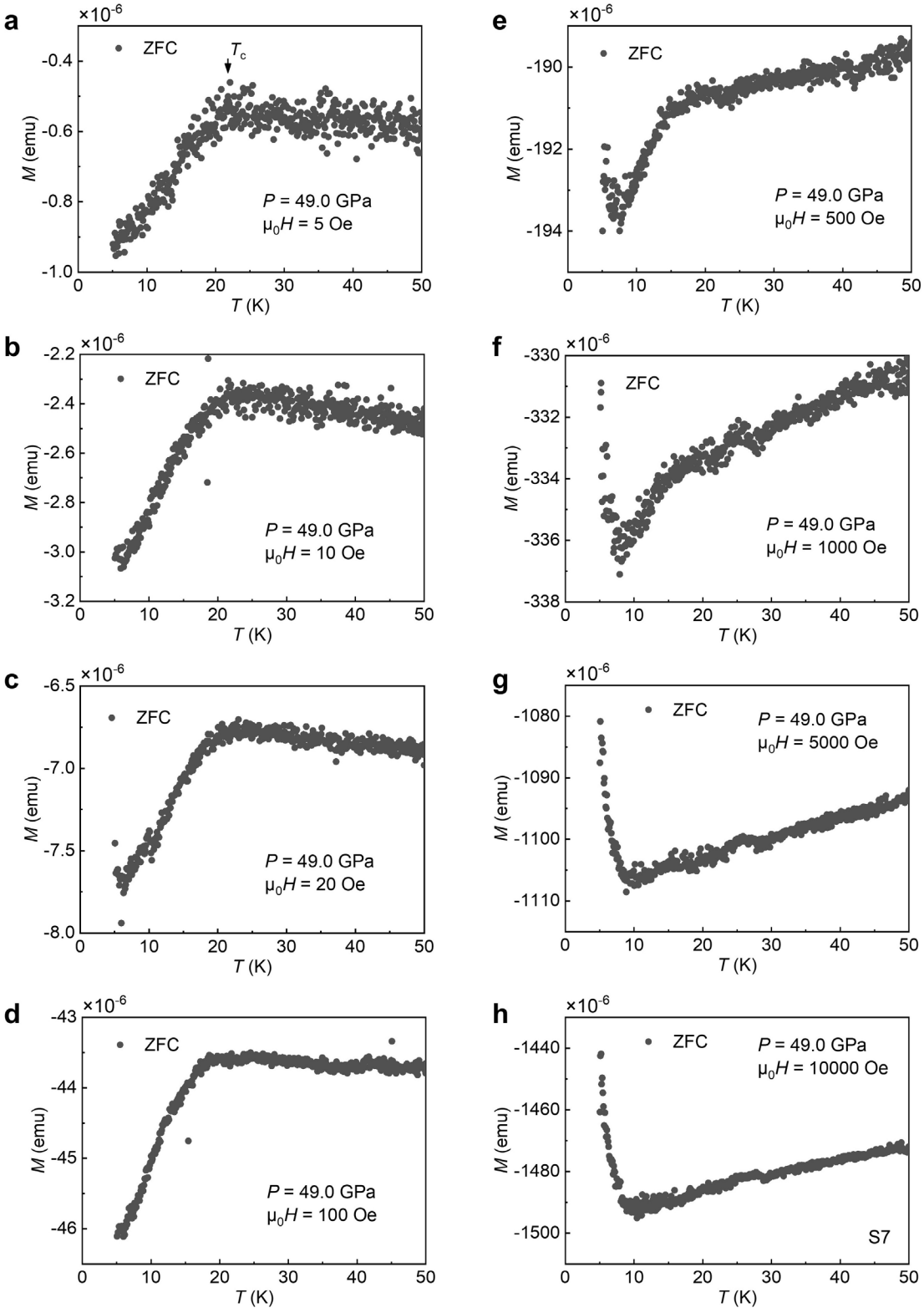

Supplementary Fig. 4｜ Temperature dependent magnetization curves for sample 7 (S7) at 49.0 GPa under the external magnetic fields of **a**, 5 Oe; **b**, 10 Oe; **c**, 20 Oe; **d**, 100 Oe; **e**, 500 Oe; **f**, 1000 Oe; **g**, 5000 Oe; **h**, 10000 Oe. Superconducting diamagnetic signals are distinctly visible at lower fields. However, as the magnetic field increases, the background magnetic signal from the pressure cell increases rapidly, making it difficult to discern the superconducting diamagnetic signal at fields above 10000 Oe.

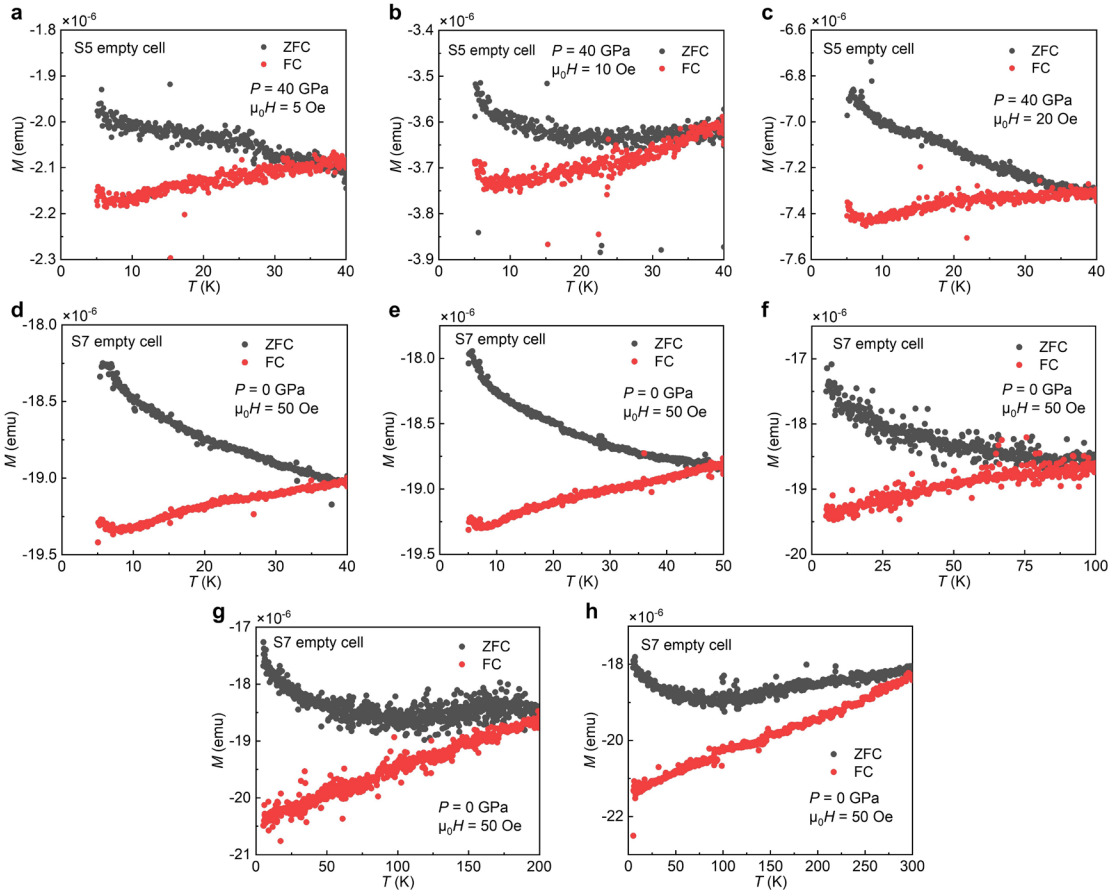

Supplementary Fig. 5| Temperature dependent magnetization curves of the empty mini-cell used for sample 5 (S5) run at 40 GPa and **a**, 5 Oe; **b**, 10 Oe; **c** 20 Oe. Temperature dependent magnetization curves of the empty cell used for sample 7 (S7) run at ambient pressure and 50 Oe within **d**, 5-40 K; **e**, 5-50 K; **f**, 5-100 K; **g**, 5-200 K; **h**, 5-300 K. The magnetic fields are applied perpendicular to the *ab* plane using the zero-field-cooled (ZFC) and field-cooled (FC) modes. The pressure cell for two different runs may have slightly different amount of rhenium used as a gasket.

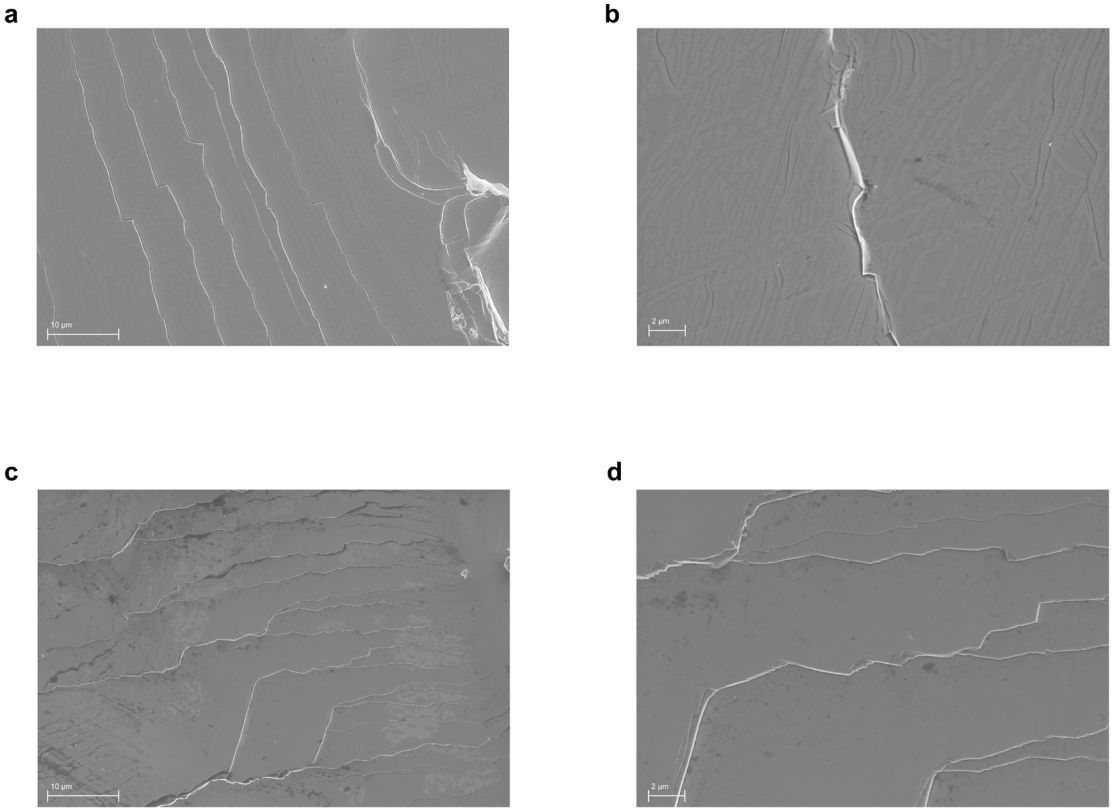

Supplementary Fig. 6 | The surface morphology of the cleavage plane of $La_4Ni_3O_{10-\delta}$ single crystals observed through scanning electron microscopy (SEM). SEM images **a**, and **c**, were obtained with a scale bar of 10 µm. Zoom-in SEM images **b**, and **d**, were obtained with a scale bar of 2 µm. Across all images, no detectable impurities were found, affirming the purity of the single crystals utilized in high-pressure resistance and susceptibility measurements.

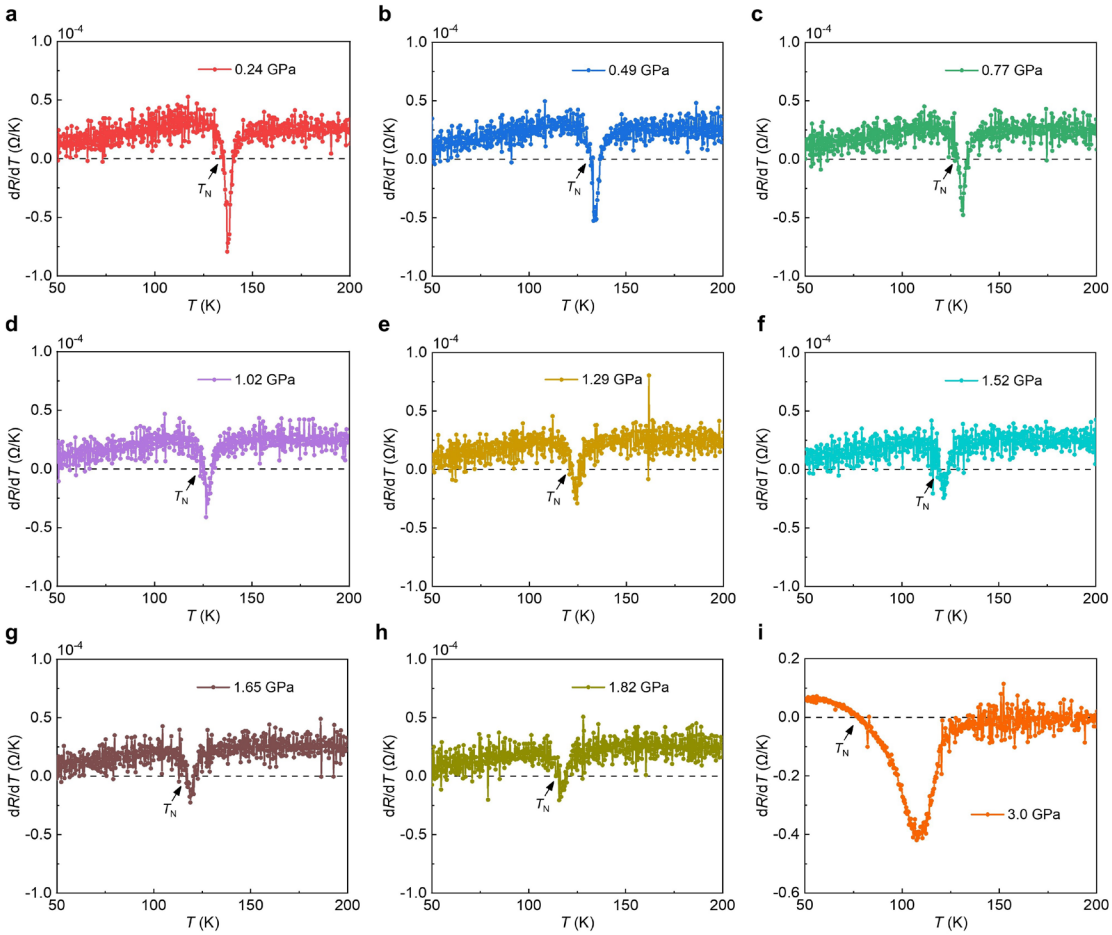

Supplementary Fig. 7 | The derivatives of the temperature-dependent resistance curves (dR/dT) derived from Figs. 3a and 3b under varying pressures. **a**, 0.24 GPa; **b**, 0.49 GPa; **c**, 0.77 GPa; **d**, 1.02 GPa; **e**, 1.29 GPa; **f**, 1.52 GPa. **g**, 1.65 GPa. **h**, 1.82 GPa. **i**, 3.0 GPa. The Néel temperature (T_N) from resistivity measurements is identified at the maximum of the resistance anomaly, where the temperature derivative dR/dT equals zero. Resistance anomalies at 11 GPa and 15.5 GPa in Fig. 3b, which are influenced by the onset of superconductivity, complicate accurate estimation of T_N and therefore are not included.

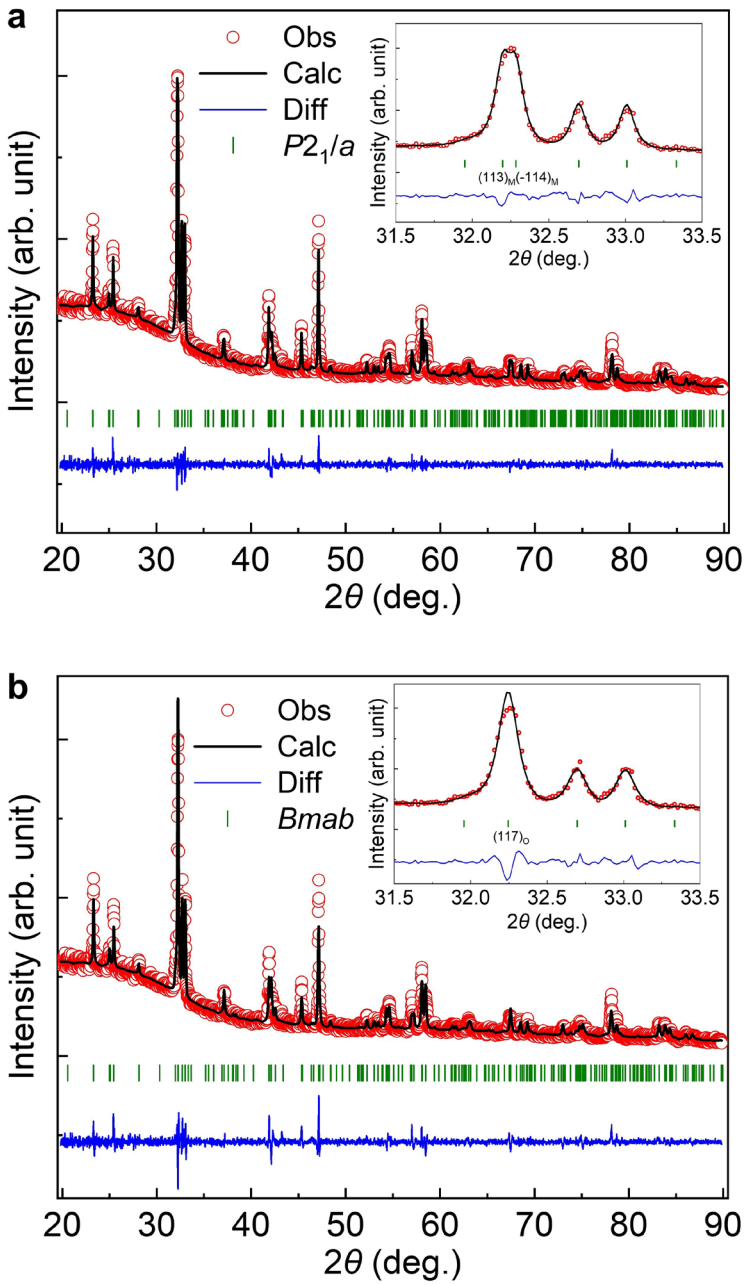

Supplementary Fig. 8 | Comparison of *P2₁/a* and *Bmab* structural models at ambient condition. **a**, Rietveld refinement of a lab-based XRD pattern for powdered $La_4Ni_3O_{10-\delta}$ single crystals at ambient pressure and room temperature. Black solid lines represent the fit to the experimental data, shown by red circles. Blue solid lines indicate the residual difference between observed and calculated intensities. Short vertical green bars mark the positions of expected Bragg peaks. This dataset fits well with the *P2₁/a* space group (GOF = 2.0, R_p = 4.12, R_{wp} = 5.46). The inset shows the details near 32.2°, where the $(1\ 1\ 3)_M$ and $(-1\ 1\ 4)_M$ peaks are captured by the *P2₁/a* model. **b**, Rietveld refinement for the *Bmab* structure using the same XRD data (GOF = 2.4, R_p = 4.74, R_{wp} = 6.62). The inset shows that the *Bmab* model fails to resolve the double peak structure near 32.2°, instead presenting a single peak of $(1\ 1\ 7)_O$ which suggests a less accurate representation of the underlying crystal structure. The measurements were carried out on a Bruker D8 Discover diffractometer, utilizing Cu Kα radiation (λ=1.5406 Å).

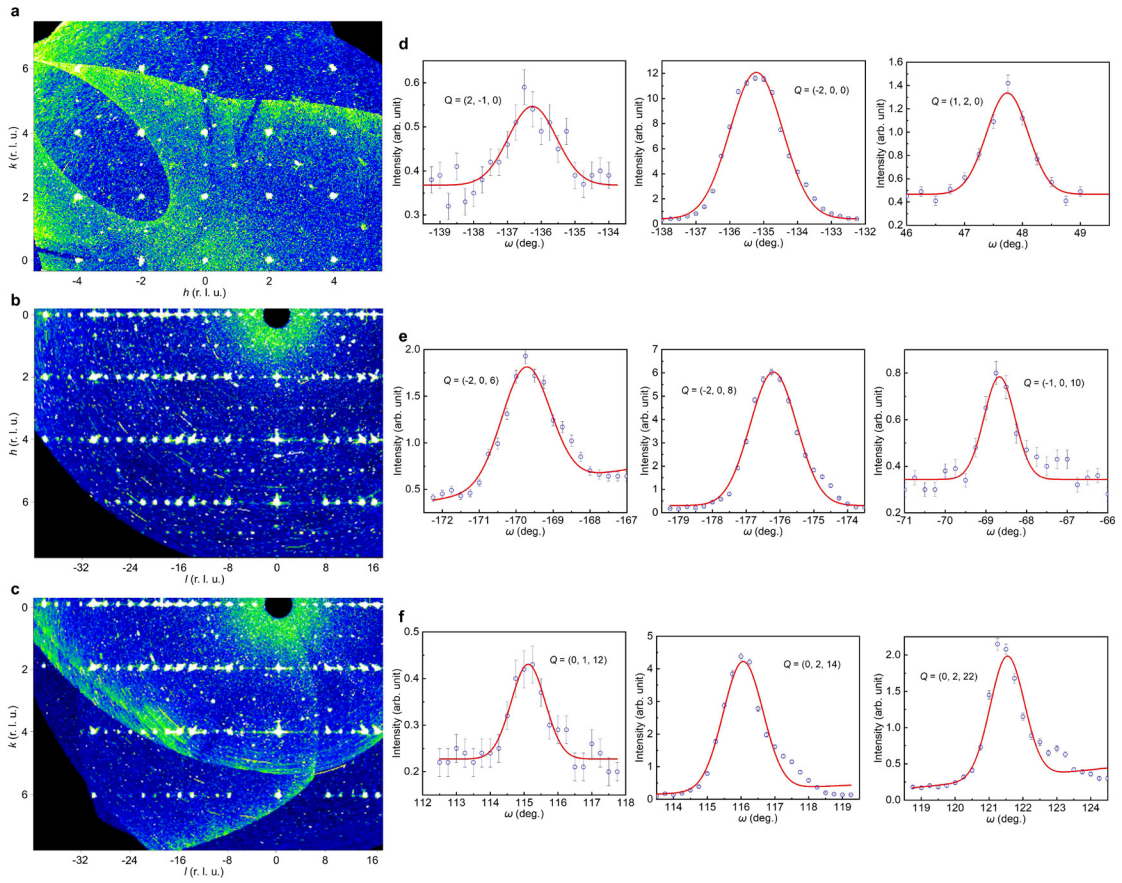

Supplementary Fig. 9 | Single-crystal X-ray and neutron diffraction measurements of $La_4Ni_3O_{10-\delta}$ at ambient pressure and room temperature. For clarity in visualizing the main Bragg peaks corresponding to both the $P2_1/a$ and *Bmab* structures, we have plotted the data based on the $P2_1/a$ structure with Z=4, having unit cell dimensions a = 5.4164 Å, b = 5.4623 Å, and c = 27.985 Å. **a**, (h k 8) reciprocal plane reconstructed from X-ray diffraction measurements. In addition to the strong Bragg peaks corresponding to the *Bmab* structure, which occur when both h and k are even, additional weaker peaks (when h k are integers) due to the monoclinic distortion inherent to the $P2_1/a$ structure are also observed. This indicates *Bmab* space group cannot accurately represent the structure; **b**, (h 0 l) reconstructed reciprocal plane; **c**, (0 k l) reconstructed reciprocal plane; **d**, Representative neutron diffraction rocking curves of the (h k 0) Bragg peaks; **e**, (h 0 l) Bragg peaks; **f**, (0 k l) Bragg peaks. The comparisons between the measured and calculated intensities of these Bragg peaks can be found in Extended Data Fig. 7a. The X-ray diffraction measurements were conducted using a lab-based Bruker D8 Venture diffractometer, while the neutron diffraction measurements utilized the HB-3A four-circle single-crystal neutron diffractometer. Error bars, 1 s.d.

Supplementary Table 1 Crystallographic parameters derived from a combined single-crystal refinement of neutron and X-ray diffractions on $La_4Ni_3O_{9.96}$ single crystals, at ambient pressure and room temperature. All O occupancies are constrained between 0 and 1.

		***P*2$_1$/*a* (*Z* = 2)**		
	a = 5.4164(3) Å	b = 5.4623(3) Å	c = 14.2279(2) Å	
	α = 90°	β = 100.75°	γ = 90°	
		Atomic positions		
Name (site)	***x***	***y***	***z***	***Occ***
La1 (4e)	0.803(1)	0.508(1)	0.103(1)	1.00
La2 (4e)	0.939(1)	0.500(1)	0.364(1)	1.00
Ni1 (2d)	0.5	0.5	0.5	1.00
Ni2 (4e)	0.862(1)	0.002(1)	0.222(1)	1.00
O1 (4e)	0.786(5)	0.967 (2)	0.068(1)	1.00
O2 (4e)	0.066(4)	0.954(2)	0.636(1)	1.00
O3 (4e)	0.112(4)	0.742(5)	0.231(1)	1.00
O4 (4e)	0.113(4)	0.248(6)	0.211(1)	0.98(2)
O5 (4e)	0.771(4)	0.723(4)	0.486(1)	1.00

R_F = 2.99, R_{F2} = 4.10, R_{wF2} = 7.32

Supplementary Table 2 Crystallographic parameters obtained from the single-crystal refinement of XRD data in $La_4Ni_3O_{10-\delta}$, conducted at 19.5 GPa and room temperature. A methanol-ethanol-water mixture in the ratio of 16:3:1 was used as the pressure-transmitting medium for the measurement.

***I*4/*mmm* (*Z* = 2)**			
a = 3.73(1) Å	b = 3.73(1) Å	c = 27.2(1) Å	
α = 90°	β = 90°	γ = 90°	
Atomic positions			
Name (site)	***x***	***y***	***z***
La1 (4e)	1.0	1.0	0.432(1)
La2 (4e)	1.0	1.0	0.302(1)
Ni1 (2a)	0.5	0.5	0.5
Ni2 (4e)	0.5	0.5	0.358(1)
O1 (8g)	1	0.5	0.363(1)
O2 (4e)	0.5	0.5	0.392(8)
O3 (4c)	0	0.5	0.5
O4 (4e)	0.5	0.5	0.281(2)

R_F = 6.25, R_{F2} = 9.28, R_{wF2} = 14.8

Supplementary Table 3 Crystallographic parameters of pressurized $La_4Ni_3O_{10-\delta}$ obtained from Rietveld refinements of high-pressure synchrotron XRD. Helium was used as the pressure-transmitting medium for the measurement.

Pressure (GPa)	a(Å)	b(Å)	c(Å)	β(°)	GOF	R_p (%)	R_{wp} (%)	Space group
0	5.4142(4)	5.4647(4)	14.220(1)	100.66	0.99	5.66	6.88	$P2_1/a$
2.5	5.3852(3)	5.4321(3)	14.147(1)	100.71	0.72	8.03	7.11	$P2_1/a$
3.5	5.3769(40)	5.4111(39)	14.127(12)	100.67	0.22	9.69	9.30	$P2_1/a$
5.0	5.3675(8)	5.3962(8)	14.100(3)	100.75	0.79	9.19	7.86	$P2_1/a$
6.5	5.3478(4)	5.3824(4)	14.085(1)	100.80	1.2	10.9	10.4	$P2_1/a$
8.3	5.3320(6)	5.3522(8)	13.983(2)	100.67	1.0	8.68	8.63	$P2_1/a$
10.0	5.3250(5)	5.3406(5)	13.972(1)	100.76	0.93	10.4	8.91	$P2_1/a$
11.7	5.2950(4)	5.3265(5)	13.910(1)	100.66	0.72	8.00	6.91	$P2_1/a$
13.7	3.7485(6)	3.7485(6)	27.346(5)	90	1.0	7.15	7.55	$I4/mmm$
15.2	3.7310(1)	3.7310(1)	27.207(1)	90	0.88	7.13	6.91	$I4/mmm$
17.2	3.7245(1)	3.7245(1)	27.130(1)	90	0.85	7.46	7.19	$I4/mmm$
18.7	3.7177(6)	3.7177(6)	27.053(5)	90	0.72	7.13	6.53	$I4/mmm$
21.6	3.7121(1)	3.7121(1)	27.023(2)	90	0.61	6.50	5.86	$I4/mmm$
24.0	3.6934(1)	3.6934(1)	26.880(1)	90	0.78	5.92	5.94	$I4/mmm$
27.1	3.6879(1)	3.6879(1)	26.854(2)	90	0.75	7.15	6.92	$I4/mmm$
30.0	3.6716(1)	3.6716(1)	26.704(2)	90	0.86	7.82	7.90	$I4/mmm$
34.0	3.6602(1)	3.6602(1)	26.609(2)	90	0.68	7.00	6.44	$I4/mmm$
38.0	3.6487(2)	3.6487(1)	26.534(2)	90	1.3	9.1	8.9	$I4/mmm$
42.0	3.6319(1)	3.6319(1)	26.452(2)	90	1.1	8.99	8.75	$I4/mmm$
48.0	3.6169(1)	3.6169(1)	26.316(1)	90	0.94	8.14	7.97	$I4/mmm$
52.0	3.6068(1)	3.6068(1)	26.243(1)	90	0.88	7.82	7.51	$I4/mmm$
56.0	3.5957(1)	3.5957(1)	26.186(2)	90	0.95	6.62	6.83	$I4/mmm$